

The clustering of galaxies in the SDSS-III Baryon Oscillation Spectroscopic Survey: Baryon Acoustic Oscillations in the correlation function of LOWZ and CMASS galaxies in Data Release 12

Antonio J. Cuesta^{1*}, Mariana Vargas-Magaña^{2,3,4}, Florian Beutler^{5,6}, Adam S. Bolton⁷, Joel R. Brownstein⁷, Daniel J. Eisenstein⁸, Héctor Gil-Marín⁹, Shirley Ho^{3,4}, Cameron K. McBride⁸, Claudia Maraston⁹, Nikhil Padmanabhan¹⁰, Will J. Percival⁹, Beth A. Reid^{5,6}, Ashley J. Ross¹¹, Nicholas P. Ross^{12,13}, Ariel G. Sánchez¹⁴, David J. Schlegel^{5,6}, Donald P. Schneider^{15,16}, Daniel Thomas⁹, Jeremy Tinker¹⁷, Rita Tojeiro¹⁸, Licia Verde^{1,19,20,21} and Martin White^{5,6,22,23}

¹*Institut de Ciències del Cosmos (ICCUB), Universitat de Barcelona (IEEC-UB), Martí i Franquès 1, E08028 Barcelona, Spain*

²*Instituto de Física, UNAM, P.O. Box 20-364, 01000 México D.F., Mexico*

³*Bruce and Astrid McWilliams Center for Cosmology, Department of Physics, Carnegie Mellon University, 5000 Forbes Ave., Pittsburgh, PA 15213, USA*

⁴*Department of Physics, Carnegie Mellon University, 5000 Forbes Ave., Pittsburgh, PA 15217*

⁵*Berkeley Center for Cosmological Physics, Department of Physics, University of California, Berkeley, CA, 94720, USA*

⁶*Lawrence Berkeley National Lab, 1 Cyclotron Rd, Berkeley, CA 94720, USA*

⁷*Department of Physics and Astronomy, University of Utah, 115 S 1400 E, Salt Lake City, UT 84112, USA*

⁸*Harvard University, Harvard-Smithsonian Center for Astrophysics, 60 Garden St., Cambridge, MA 02138, USA*

⁹*Institute of Cosmology & Gravitation, Dennis Sciama Building, University of Portsmouth, Portsmouth, PO1 3FX, UK*

¹⁰*Department of Physics, Yale University, 260 Whitney Avenue, New Haven, CT 06520, USA*

¹¹*Center for Cosmology and AstroParticle Physics, The Ohio State University, Columbus, OH 43210, USA*

¹²*Institute for Astronomy, University of Edinburgh, Royal Observatory, Blackford Hill Edinburgh EH9 3HJ, United Kingdom*

¹³*Department of Physics, Drexel University, 3141 Chestnut Street, Philadelphia, PA 19104, USA*

¹⁴*Max-Planck-Institut für Extraterrestrische Physik, Giessenbachstrasse 1, D-85748 Garching, Germany*

¹⁵*Department of Astronomy and Astrophysics, The Pennsylvania State University, University Park, PA 16802*

¹⁶*Institute for Gravitation and the Cosmos, The Pennsylvania State University, University Park, PA 16802*

¹⁷*Center for Cosmology and Particle Physics, Department of Physics, New York University*

¹⁸*School of Physics and Astronomy, University of St Andrews, North Haugh, St Andrews KY16 9SS, UK*

¹⁹*ICREA (Institució Catalana de Recerca i Estudis Avançats)*

²⁰*Radcliffe Institute for Advanced Study, Harvard University, MA 02138, USA*

²¹*Institute of Theoretical Astrophysics, University of Oslo, 0315 Oslo, Norway*

²²*Department of Astronomy, University of California, Berkeley, CA 94720, USA*

²³*Department of Physics, University of California, Berkeley, CA 94720, USA*

12 January 2016

ABSTRACT

We present distance scale measurements from the baryon acoustic oscillation signal in the CMASS and LOWZ samples from the Data Release 12 of the Baryon Oscillation Spectroscopic Survey (BOSS). The total volume probed is 14.5 Gpc³, a 10 per cent increment from Data Release 11. From an analysis of the spherically averaged correlation function, we infer a distance to $z = 0.57$ of $D_V(z)r_d^{\text{fid}}/r_d = 2028 \pm 21$ Mpc and a distance to $z = 0.32$ of $D_V(z)r_d^{\text{fid}}/r_d = 1264 \pm 22$ Mpc assuming a cosmology in which $r_d^{\text{fid}} = 147.10$ Mpc. From the anisotropic analysis, we find an angular diameter distance to $z = 0.57$ of $D_A(z)r_d^{\text{fid}}/r_d = 1401 \pm 21$ Mpc and a distance to $z = 0.32$ of 981 ± 20 Mpc, a 1.5 per cent and 2.0 per cent measurement respectively. The Hubble parameter at $z = 0.57$ is $H(z)r_d/r_d^{\text{fid}} = 100.3 \pm 3.7$ km s⁻¹ Mpc⁻¹ and its value at $z = 0.32$ is 79.2 ± 5.6 km s⁻¹ Mpc⁻¹, a 3.7 per cent and 7.1 per cent measurement respectively. These cosmic distance scale constraints are in excellent agreement with a Λ CDM model with cosmological parameters released by the recent *Planck* 2015 results.

Key words: cosmology: observations, distance scale, large-scale structure of Universe

1 INTRODUCTION

The Data Release 12 (DR12, Alam et al. 2015)¹ of the Baryon Oscillation Spectroscopic Survey (BOSS, Dawson et al. 2013) represents a major milestone in the history of baryon acoustic oscillation (BAO) observations, and in general, of cosmic distance scale measurements. The unprecedented precision goal of 1 per cent in a cosmological distance was achieved in Data Release 11 (Anderson et al. 2014) and has not been matched since then, even by local expansion rate measurements. Improvements are expected in the next few years extending to higher redshifts with the extended BOSS survey (Dawson et al. 2015) and HETDEX (Hill et al. 2008). Substantial improvements are not expected until results are available from the next generation of experiments, including EUCLID (Laureijs 2009; Laureijs et al. 2011), LSST (LSST Dark Energy Science Collaboration 2012), SKA (Bull et al. 2015), WFIRST (Spergel et al. 2013a,b), and DESI (Mostek et al. 2012; Levi et al. 2013).

This breakthrough is the continuation of a ten-year history of BAO observations. Early BAO measurements by Eisenstein et al. (2005), using a previous incarnation of the SDSS survey, and Cole et al. (2005), using the 2dF survey, paved the way for modern BAO measurements from galaxy surveys such as the 6dFGS (Beutler et al. 2011) and WiggleZ (Blake et al. 2011). Later measurements reconstructed the linear density field in order to improve distance scale constraints (Eisenstein et al. 2007; Padmanabhan et al. 2012), including existing distance measurements (Padmanabhan et al. 2012; Kazin et al. 2014; Ross et al. 2015) and the new BOSS measurements (Anderson et al. 2012, 2014).

BOSS has populated the distance-redshift diagram with four new data points, two from the clustering of galaxies (Tojeiro et al. 2014; Anderson et al. 2014) and two from the two-point function of the transmission flux in the Lyman- α forest (Font-Ribera et al. 2014a; Delubac et al. 2015). The enormous volume probed by these samples has been key to providing low-uncertainty distance scale measurements, which have become an invaluable input for most state-of-the-art cosmological analyses.

Baryon acoustic oscillations distance measurements using BOSS galaxies have traditionally been determined using two different galaxy samples: The ‘‘Constant Stellar Mass’’ sample, or CMASS, covering redshifts in the range $0.43 < z < 0.70$ and a fiducial redshift of 0.57, and the low-redshift sample, or LOWZ, covering redshifts of $0.15 < z < 0.43$ with an effective redshift of 0.32 (Reid et al. 2016, companion paper).

The Data Release 12 represents an increment of 10 per cent in area, volume, and number of galaxies over Data Release 11. The main paper Anderson et al. (2016, in preparation) (hereafter the *Final Data Release* paper) offers an analysis of the same DR12 sample not split into LOWZ and CMASS, but combined optimally together. Here instead as part of the BOSS legacy, we present the distance scale measurements from the traditional LOWZ and CMASS measurements, which serve a two-fold purpose. The constraining power of the results in Anderson et al. (2016, in preparation) can be tested against the traditional analysis (this paper), hence being a benchmark of the new analysis techniques.

Table 1. Statistics of the LOWZ and CMASS galaxy samples used in this paper.

	NGC	SGC	Total
LOWZ	248,237	113,525	361,762
CMASS	568,776	208,426	777,202
LOWZ+CMASS	817,013	321,951	1,138,964

Moreover, the results presented here can be readily compared with previous BOSS Data Releases, which provides more transparency to our final results.

This analysis not only benefits from new data. We also take advantage from an updated version of the systematic weights (Ross et al. 2016, in preparation) to account for spurious large scale fluctuations in the galaxy number density due to observational systematic effects. We have also updated the set of mocks to compute the covariance matrix to the new Quick-Particle-Mesh, or QPM, mocks (White, Tinker & McBride 2014). The QPM mocks, which are generated using a new methodology and with a cosmology closer to current constraints than the mocks used in DR11, result in an improved measurement not only in terms of the formal statistical errors and covariances but also offer a reliable, more robust determination of the cosmic distance scale and its uncertainty.

This paper is organized as follows: in Section 2 we describe the final statistics of the LOWZ and CMASS samples of BOSS. Section 3 discusses the mocks and tests our fitting techniques. Section 4 presents the results of the isotropic and anisotropic fittings of the two-point function of LOWZ and CMASS in configuration space (and compares them with those in Fourier space), Section 5 discusses the cosmological implications of these distance measurements, and Section 6 summarizes our conclusions.

2 DATASETS

This paper uses data from the Data Release 12 (Alam et al. 2015) of the Baryon Oscillation Spectroscopic Survey (BOSS) (Eisenstein et al. 2011). The BOSS survey uses the SDSS 2.5 meter telescope at Apache Point Observatory (Gunn et al. 2006) and the spectra are obtained using the double-armed BOSS spectrograph (Smee et al. 2013). The data are then reduced using the algorithms described in Bolton et al. (2012).

The target selection of the CMASS and LOWZ samples, together with the algorithms used to create large scale structure catalogues (the MKSAMPLE code), are presented in the companion paper Reid et al. (2016).

The LOWZ sample contains 361,762 galaxies in the range $0.15 < z < 0.43$, with 248,237 in the North Galactic Cap (NGC) and 113,525 in the South Galactic Cap (SGC). The CMASS sample contains 777,202 galaxies in the range $0.43 < z < 0.70$, with 568,776 in the NGC and 208,426 in the SGC. This total of 1,138,964 galaxies is used in our analysis (see Table 1).

The area covered by these samples is shown in Table 2, including a comparison with the coverage in Data Release 11. The sky coverage in CMASS sample has increased by 11.9 per cent whereas that of the LOWZ sample

¹ <http://sdss.org/dr12>

Table 2. Sky coverage in LOWZ and CMASS samples (effective area, in deg²).

	NGC	SGC	Total
LOWZ DR11	5290.82	2050.60	7341.42
LOWZ DR12	5836.21	2501.26	8337.47
CMASS DR11	6307.94	2068.96	8376.90
CMASS DR12	6851.42	2524.67	9376.09

Table 3. Effective volume (in Gpc³) of the LOWZ and CMASS samples for different values of the matter density Ω_m , the Hubble parameter h , and the amplitude of the matter power spectrum at the BAO scale P_0 .

	LOWZ	CMASS	Total
$P_0 = 20,000 h^{-3} \text{Mpc}^3$			
$\Omega_m = 0.274, h = 0.700$	2.65	6.65	9.30
$\Omega_m = 0.290, h = 0.700$	2.62	6.55	9.17
$\Omega_m = 0.310, h = 0.676$	2.87	7.14	10.01
$P_0 = 10,000 h^{-3} \text{Mpc}^3$			
$\Omega_m = 0.274, h = 0.700$	2.00	4.70	6.70
$\Omega_m = 0.290, h = 0.700$	1.98	4.65	6.63
$\Omega_m = 0.310, h = 0.676$	2.18	5.11	7.29

has increased by 13.6 per cent. The LOWZ area is slightly smaller than the CMASS area mainly because some regions of LOWZ were targeted with a different selection (Reid et al. 2016, companion paper). Those regions however will be included in the analysis shown in Anderson et al. (2016, in preparation).

The total volume (assuming our fiducial cosmology described in Section 3) that the LOWZ and CMASS galaxies occupy amounts to a total of 14.5 Gpc³, out of which 10.8 Gpc³ corresponds to CMASS and 3.7 Gpc³ corresponds to LOWZ. We also compute the effective volume V_{eff} , defined as:

$$V_{\text{eff}} = \int dV \left(\frac{n(z)P_0}{1 + n(z)P_0} \right)^2 \quad (1)$$

where P_0 is an estimate of the amplitude of the power spectrum at the BAO scale, here assumed to be $P_0 = 20,000 h^{-3} \text{Mpc}^3$ (as in Anderson et al. 2014), and $n(z)$ is the galaxy number density. In Anderson et al. (2016, in preparation) the value used is $10,000 h^{-3} \text{Mpc}^3$ following Font-Ribera et al. (2014b). For a comparison of volumes in different cosmologies and P_0 values see Table 3.

We then compute the FKP-weighted (Feldman, Kaiser & Peacock 1994) correlation functions using the Landy-Szalay estimator (Landy & Szalay 1993), with a random catalogue² generated by the MKSAMPLE code (see Reid et al. 2016, companion paper) to match the geometry, redshift distribution, and completeness of the survey. These functions include the corrections for systematic effects described in

² The size of the random catalogue is 50 times the size of the data samples, and in the case of the QPM mocks we use 20 times the size of the mock catalogues.

Ross et al. (2016, in preparation), which account for correlations between the observed galaxy density of the CMASS sample and stellar density in the sky and seeing. We also include weights that correct for close pairs (fibre collisions) and redshift failures in these samples. A detailed description of the observational systematic weights and their effect on the measured clustering will be provided in Ross et al. (2016, in preparation). As shown in Ross et al. (2012), these weights compensate for the systematic effect by interpolating the observed deficit in the number density of galaxies as a function of the systematic, and weighting by the inverse of this deficit. The systematic that has a larger effect in the measured correlation function is stellar density, with seeing providing a more modest correction. Fibre collision weights are very significant at small scales, although their contribution to the clustering is negligible at the BAO scale. Redshift failure weights also show a rather small effect in the measured clustering. Again, this topic will be revisited in the context of the DR12 samples in Ross et al. (2016, in preparation), where any impact on the measured BAO scale is found to be negligible. The resulting correlation functions for CMASS and LOWZ are shown in Figure 1, where we display the pre-reconstruction correlation functions with a dashed line. As in Anderson et al. (2014), we also apply density field reconstruction (Padmanabhan et al. 2012) to our samples, which we test on mock galaxy samples in Section 3. The resulting post-reconstruction correlation functions are plotted with a solid line. Also displayed for reference is the correlation function from the previous Data Release 11 (re-computed using the fiducial cosmology used in this paper) with a fainter line.

3 METHODOLOGY

The mock catalogues and error estimates are computed with a fiducial cosmology that is close to the best-fit Planck+BOSS cosmology, such that they faithfully produce the covariances and fitting errors of the data. Our fiducial cosmology is given by the following set of cosmological parameters³: $\Omega_m = 0.29$, $\Omega_\Lambda = 0.71$, $\Omega_k = 0$, $\Omega_b h^2 = 0.02247$, $\Omega_\nu h^2 = 0.0$, $w = -1$, $w_a = 0$, $h = 0.7$, $n_s = 0.97$, and $\sigma_8 = 0.8$. The choice of this cosmology is motivated by our Planck+BAO (i.e. Planck+LOWZ+CMASS+6dF+LyA) constraints in Anderson et al. (2014) in the Λ CDM model, and the fact that the fiducial cosmology in Anderson et al. (2014) corresponds to a value of $\Omega_m h^3$ that lies more than 6σ away from the tight constraints from Planck Cosmic Microwave Background data (Planck Collaboration et al. 2015b). In this fiducial cosmology⁴, the volume-averaged

³ This is a slightly different choice from that of the Final Data Release paper (Anderson et al. 2016, in preparation) in which $\Omega_m = 0.31$, $\Omega_\Lambda = 0.69$, $\Omega_k = 0$, $\Omega_b h^2 = 0.022$, $\Omega_\nu h^2 = 0.00064$, $w = -1$, $w_a = 0$, $h = 0.676$, $n_s = 0.97$, and $\sigma_8 = 0.8$

⁴ For comparison, in the fiducial cosmology of Anderson et al. (2016, in preparation) the volume-averaged distance to redshift $z = 0.32$ is $D_V(0.32) = 1271.2215 \text{Mpc}$, $D_A(0.32) = 991.9952 \text{Mpc}$, $H(0.32) = 80.07077 \text{km s}^{-1} \text{Mpc}^{-1}$, the distance to redshift $z = 0.57$ is $D_V(0.57) = 2059.5562 \text{Mpc}$, $D_A(0.57) = 1388.298 \text{Mpc}$, $H(0.57) = 92.92644 \text{km s}^{-1} \text{Mpc}^{-1}$ and the sound horizon scale is $r_{\text{d,fid}} = 147.781 \text{Mpc}$.

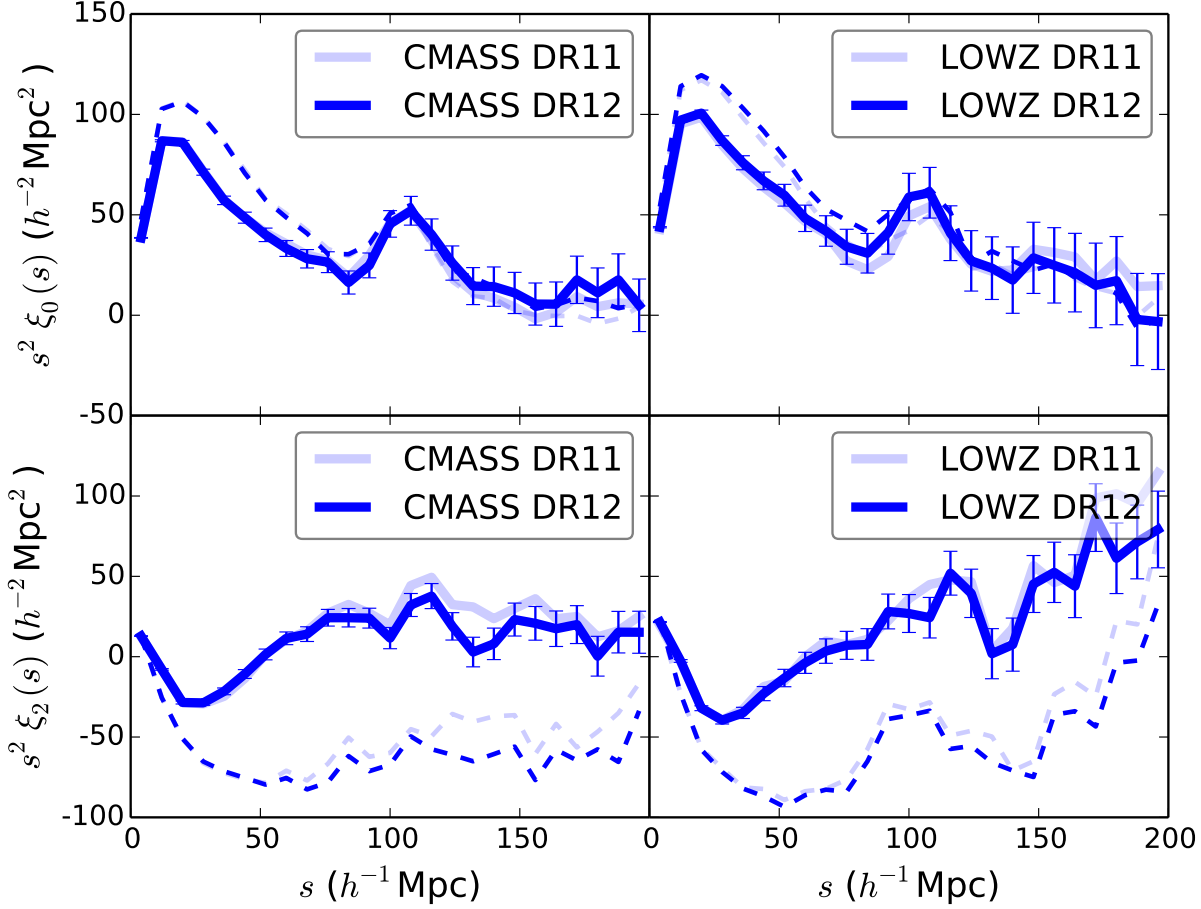


Figure 1. Monopole (top) and quadrupole (bottom) of the CMASS and LOWZ correlation functions assuming our fiducial cosmology. Left panels show the CMASS correlation function, whereas right panels present the LOWZ correlation function. In all panels the dashed line indicates the correlation function pre-reconstruction. The lighter shade is the DR11 version for comparison. Error bars represent the square root of the diagonal elements of the covariance matrix.

distance to redshift $z = 0.32$ is $D_V(0.32) = 1235.28$ Mpc, $D_A(0.32) = 962.43$ Mpc, $H(0.32) = 82.142$ km s $^{-1}$ Mpc $^{-1}$, the distance to redshift $z = 0.57$ is $D_V(0.57) = 2009.55$ Mpc, $D_A(0.57) = 1351.13$ Mpc, $H(0.57) = 94.753$ km s $^{-1}$ Mpc $^{-1}$ and the sound horizon scale is $r_{d,\text{fid}} = 147.10$ Mpc. The sound horizon is evaluated using CAMB (Lewis, Challinor & Lasenby 2000)⁵.

The fiducial value of the sound horizon scale used in the analysis in Anderson et al. (2014) ($r_{d,\text{fid}} = 149.28$ Mpc) is now ruled out by more than 6σ from its inferred value using Planck temperature and polarization data in a Λ CDM model where the effective number of relativistic species is set to the standard value of $N_{\text{eff}} = 3.046$. The fiducial value used in Anderson et al. (2016, in preparation) is $r_{d,\text{fid}} = 147.78$ Mpc, consistent with the constraints from the Planck observations for a standard Λ CDM model.

The analysis of the clustering of galaxies in Data Release 12 uses two sets of mocks in order to estimate the

covariance matrix. These are the QPM mocks (White, Tinker & McBride 2014) and the MultiDark-Patchy BOSS DR12 mocks, hereafter MD-Patchy⁶ (Kitaura et al. 2015, -companion paper-, Kitaura, Yepes & Prada 2014). Both were generated to match the footprint and number density of the CMASS and LOWZ samples from Data Release 12. We have fitted the DR12 correlation function using both covariance matrices; the QPM mocks return a slightly larger error bar. Since we find no compelling reason to choose one set of mocks over the other, we will adopt a conservative approach and from now on we discuss the results that quote a larger statistical uncertainty, corresponding to those using the QPM covariance matrix only. The values of cosmological parameters for both cosmologies are shown in Table 4 and the fiducial distances to $z = 0.32$ and $z = 0.57$ in Table 5.

The data catalogues have been carefully tested for systematics. A thorough study of systematics in LOWZ and CMASS galaxy samples is presented in Ross et al. (2016, in preparation). All the systematic effects found to correlate

⁵ <http://camb.info>

⁶ <http://data.sdss3.org/datamodel/index-files.html>

Table 4. Cosmological parameters of the QPM and MD-Patchy mock catalogues. Our choice for the fiducial cosmology corresponds to the cosmology of the QPM mocks. For comparison we include the values corresponding to the fiducial cosmology in Anderson et al. (2016).

	h	$\Omega_b h^2$	Ω_m	Ω_Λ	n_s	σ_8
QPM & this work	0.7	0.02247	0.29	0.71	0.97	0.8
MD-Patchy	0.6777	0.02214	0.307115	0.692885	0.9611	0.8288
Anderson et al. (2016)	0.676	0.022	0.31	0.69	0.97	0.8

Table 5. Fiducial distances and Hubble parameters for the cosmologies of the QPM and MD-Patchy mock catalogues, computed at the fiducial redshifts of LOWZ ($z = 0.32$) and CMASS ($z = 0.57$) assuming a Λ CDM cosmological model. Our choice for the fiducial cosmology corresponds to the cosmology of the QPM mocks. The sound horizon at radiation drag r_d was evaluated using CAMB. For comparison we include the values corresponding to the fiducial cosmology in Anderson et al. (2015).

	r_d (Mpc)	$D_A(z = 0.32)$ (Mpc)	$H(z = 0.32)$ (km s $^{-1}$ Mpc $^{-1}$)	$D_V(z = 0.32)$ (Mpc)	$D_A(z = 0.57)$ (Mpc)	$H(z = 0.57)$ (km s $^{-1}$ Mpc $^{-1}$)	$D_V(z = 0.57)$ (Mpc)
QPM & this work	147.10	962.43	82.142	1235.28	1351.13	94.753	2009.55
MD-Patchy	147.66	990.16	80.165	1269.16	1386.35	92.956	2057.41
Anderson et al. (2016)	147.78	992.00	80.071	1271.22	1388.30	92.926	2059.56

with galaxy density of these samples are compensated by assigning weights to each galaxy. After including all these systematic weights, and combining them with the corrections from close pairs and redshift failures, we compute the clustering of the resulting samples in our fiducial cosmology. We adopt the reconstruction technique (Eisenstein et al. 2007) which has been applied regularly in galaxy surveys since Padmanabhan et al. (2012) to partially remove the effect of non-linearities on the uncertainties in cosmic distance measurements (Eisenstein, Seo & White 2007; Crocce & Scoccimarro 2008). A bias parameter of $b = 1.85$ for both samples (Anderson et al. 2014; Tojeiro et al. 2014) and a redshift space distortion parameter $\beta = b^{-1} d \ln D / d \ln a$ from the QPM cosmology ($\beta = 0.4128$ for the central redshift of CMASS, $\beta = 0.3628$ for LOWZ) is assumed. For the mocks, a bias of $b = 2.1$ and a value of $\beta = 0.3607$ for the central redshift of CMASS, $\beta = 0.3353$ for LOWZ are adopted. The difference in the bias is due to the relative amplitude of the clustering of the mocks and the data at scales of $30 h^{-1}$ Mpc with respect to the clustering of the dark matter in our fiducial cosmology. In all cases a Gaussian kernel of $15 h^{-1}$ Mpc is applied to smooth the galaxy density field when applying reconstruction. The effects of the particular choice of the smoothing length are studied in detail in the companion paper Vargas-Magaña et al. (2015).

Figure 2 shows the monopole and quadrupole of the QPM mock correlation functions pre-reconstruction (blue) and post-reconstruction (red) for the CMASS and LOWZ samples. The shaded region represents the standard deviation of the mock correlation functions around their average, which is displayed with a dashed line. For reference we include the observed correlation functions from Data Release 12 as dotted lines. We note that as in Anderson et al. (2014), the covariance matrix computed from the mock catalogues has been corrected using the corresponding Hartlap factors (Hartlap, Simon & Schneider 2007) for our number of mocks, number of fitting parameters, and number of bins (see Percival et al. 2014).

4 BAO FITTING RESULTS

In this section we present the results of the isotropic and anisotropic BAO fittings in this paper. We compute the correlation functions in $8 h^{-1}$ Mpc bins and consider scales in the range $30 h^{-1}$ Mpc to $180 h^{-1}$ Mpc for the fitting procedure. This binning size and fitting range is close to optimal (see Ross et al. 2016, in preparation).

We fit the correlation functions shown in Figure 1 to a template based on the matter power spectrum for our fiducial cosmology generated by the Boltzmann code CAMB (Lewis, Challinor & Lasenby 2000). We construct a template in which the correlation function for the fiducial model is convoluted with a Gaussian to reproduce the damping effect on the BAO due to non-linearities (Eisenstein, Seo & White 2007) calibrated on the average of our 1000 mocks (see Section 4.1). Hereafter this template is designated as the 'de-wiggled' template $\xi^{\text{de-wiggled}}$, which we use in our isotropic and anisotropic BAO fittings. We then marginalize over the amplitude and the smooth shape of the correlation function introducing three nuisance polynomial terms and a nuisance amplitude term. The resulting fitting function is therefore:

$$\xi^{\text{fit}}(r) = B_0^2 \xi^{\text{de-wiggled}}(\alpha r) + A_0 + \frac{A_1}{r} + \frac{A_2}{r^2} \quad (2)$$

where A_0 , A_1 and A_2 are parameters that try to capture any smooth deviation from our template due to large-scale systematics and non-linear bias, and B_0 is a normalization parameter. All these four coefficients are nuisance parameters which are marginalized over in our fittings. Further details on the fitting methodology used here can be found in Vargas-Magaña et al. (2016, in preparation).

In the anisotropic fittings we fit for both α and ϵ (see e.g. Xu et al. 2013), which are related to the angular diameter distance $D_A(z)$ and Hubble parameter $H(z)$.

$$\alpha = \frac{D_A^{2/3}(z)H^{-1/3}(z)/r_d}{\left(D_A^{2/3}(z)H^{-1/3}(z)/r_d\right)_{\text{fid}}} \quad 1 + \epsilon = \left(\frac{D_A(z)H(z)}{\left(D_A(z)H(z)\right)_{\text{fid}}}\right)^{-1} \quad (3)$$

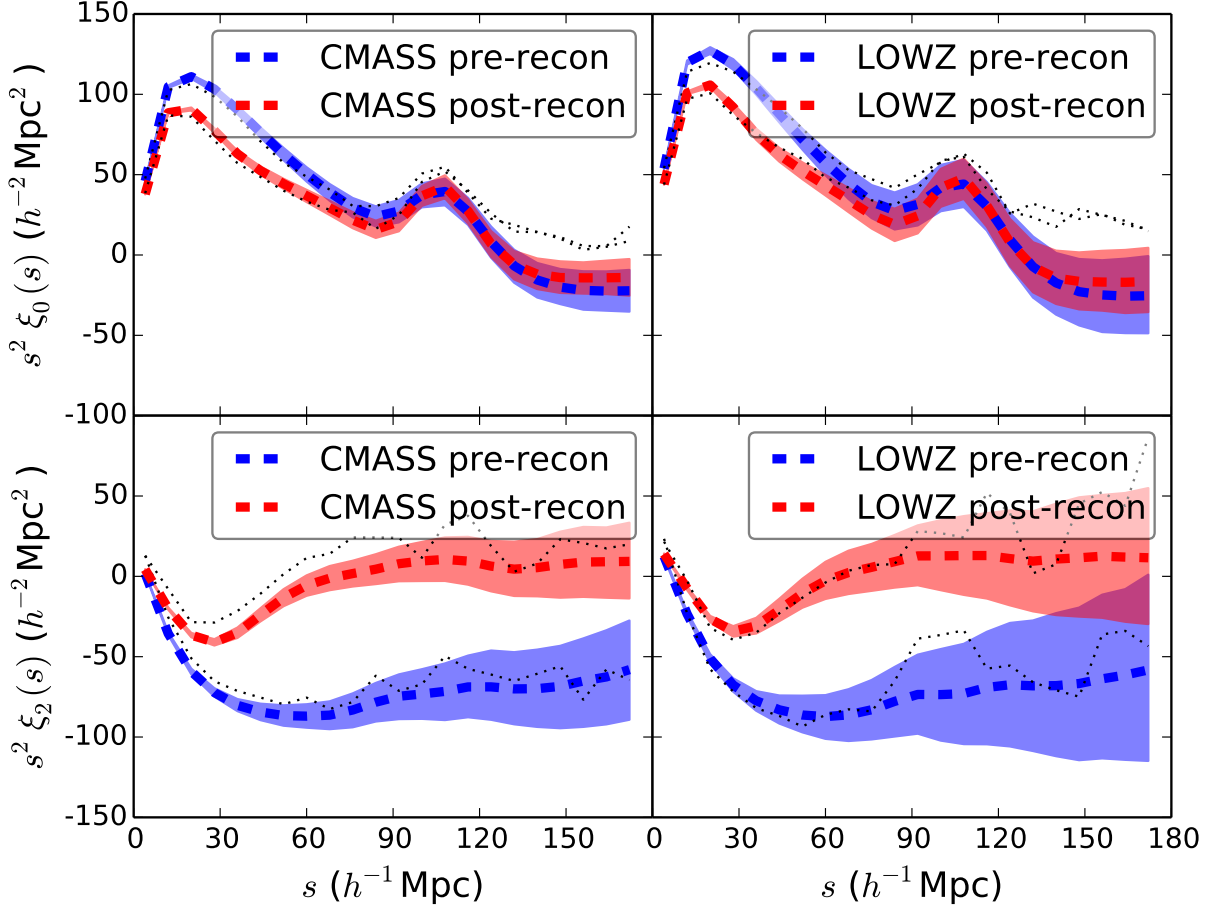


Figure 2. The correlation function of QPM mocks, pre-reconstruction (blue) and post-reconstruction (red). The upper panels show the average and standard deviation (dashed line and shaded regions) of the monopole of the CMASS (left) and LOWZ (right) correlation function of the QPM mocks. Bottom panels display the average and standard deviation of the quadrupole of the QPM correlation functions for CMASS (left) and LOWZ (right). A dotted line shows the clustering of the data for comparison.

These parameters are related to the dilation factors in the line of sight and the perpendicular directions, α_{\parallel} and α_{\perp} , as follows:

$$\alpha = \alpha_{\parallel}^{1/3} \alpha_{\perp}^{2/3} \quad 1 + \epsilon = \left(\frac{\alpha_{\parallel}}{\alpha_{\perp}} \right)^{1/3} \quad (4)$$

which in turn can be written in terms of the angular diameter distance and Hubble parameter via:

$$\alpha_{\perp} = \frac{D_A(z)/r_d}{(D_A(z)/r_d)_{\text{fid}}} \quad \alpha_{\parallel} = \left(\frac{H(z)r_d}{(H(z)r_d)_{\text{fid}}} \right)^{-1} \quad (5)$$

The isotropic fittings, which fit for the parameter α , can be used to determine the value of the angle-averaged distance $D_V(z)$, which we also report in this paper:

$$D_V(z) = [cz(1+z)^2 D_A^2(z) H^{-1}(z)]^{1/3} \quad (6)$$

A comprehensive analysis of the fitting systematics is presented in Vargas-Magaña et al. (2016, in preparation). We refer the reader to that paper for further details.

Figure 3 displays the post-reconstruction DR12 correlation functions, for CMASS (left panels) and LOWZ (right panels), together with their best-fitting models. The top panels show the monopole of the correlation function, the bottom panels present the quadrupole. The model of equation 2 fits really well the data, with a goodness of fit of $\chi^2 = 25$ for LOWZ and 26 for CMASS, for 26 degrees of freedom (36 data points minus 10 fitting parameters).

4.1 Mock fitting results

We begin with the results from fitting the QPM mocks. We use 956 mocks for the CMASS sample and 1000 for LOWZ. We compute the median and standard deviations of the geometric parameters α , ϵ , α_{\parallel} , and α_{\perp} and present them in Table 6. Since our fiducial cosmology corresponds to the input cosmology of the mocks, we expect that on average $\epsilon = 0$ and $\alpha = \alpha_{\parallel} = \alpha_{\perp} = 1$. Indeed, our recovered parameters values are not biased in any of the pre-reconstruction or post-reconstruction samples. Moreover, the scatter in the measurements provide an approximate idea of the uncertain-

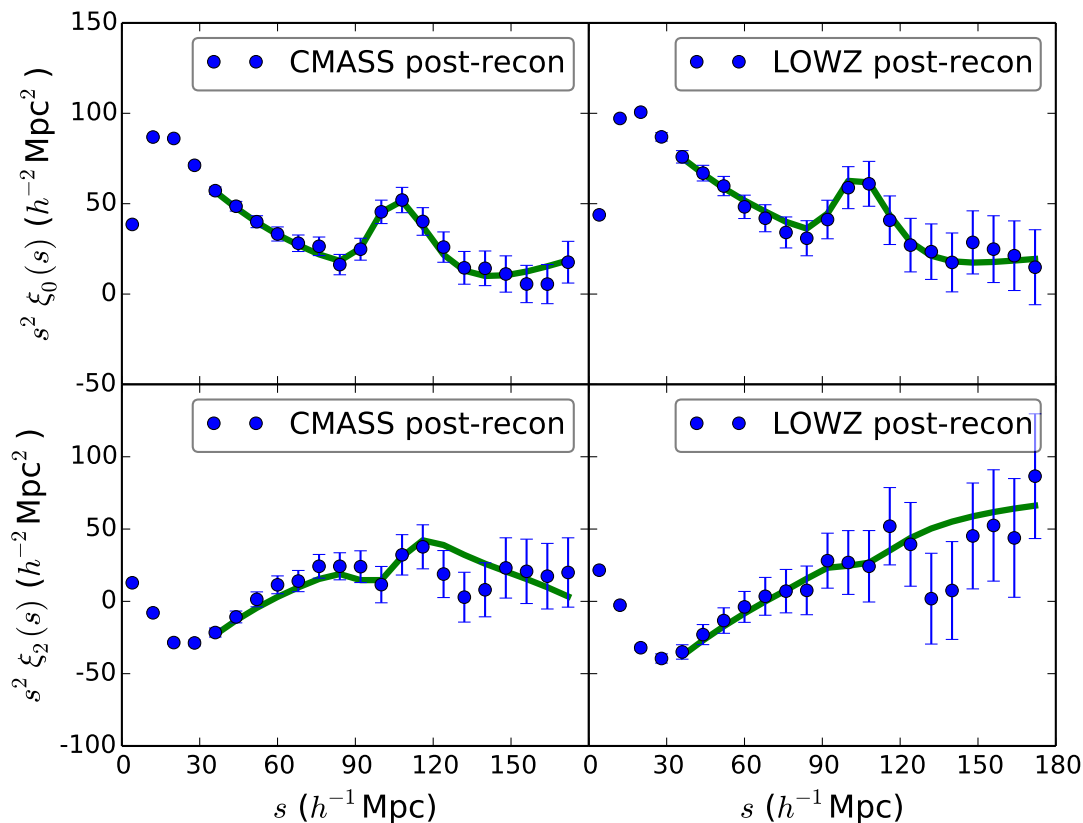


Figure 3. The correlation function of CMASS galaxies (left panels) and LOWZ galaxies (right panels). Top panels show the monopole of the correlation function post-reconstruction, bottom panels display the quadrupole of the correlation function. Error bars represent the square root of the diagonal elements of the covariance matrix. In all panels the best-fitting model is presented for reference (solid lines, see text for more details).

ties we should expect in the data. Post-reconstruction the typical uncertainty in $D_A(z)$ and $H(z)$ is 2.5 per cent and 5.2 per cent respectively for LOWZ, and is 1.6 per cent and 3.1 per cent for CMASS.

The distribution of the uncertainties recovered in the BAO fittings of the mocks are shown in Figure 5 for LOWZ and Figure 6 for CMASS, respectively. The blue lines present the distribution before applying density field reconstruction and in red lines the distribution after reconstruction. Overall there is an improvement in the uncertainties of all the geometric parameters for both LOWZ and CMASS samples after reconstruction. A mock-by-mock comparison of the performance of the reconstruction technique on individual mocks can be seen in Figure 4. In this figure each point represents a mock, and its location is given by its uncertainty pre- and post-reconstruction. The points in the region below the red line represent those mocks where reconstruction reduced the uncertainty in the corresponding parameter. In CMASS the vast majority of mocks are improved due to reconstruction, whereas a lower fraction of LOWZ mocks found that improvement. In particular, for σ_α only 3.2 per cent of the CMASS mocks (8.7 per cent of the LOWZ mocks) were not improved post-reconstruction. For σ_{α_\perp} this fraction was 1.8 per cent for CMASS (5.8 per cent for LOWZ), and

for $\sigma_{\alpha_\parallel}$ this was 6.9 per cent for CMASS (13.2 per cent for LOWZ).

4.2 Data fitting results

We now apply our isotropic and anisotropic fitting analysis to the LOWZ and CMASS Data Release 12 galaxy catalogues. The results are presented in Table 7. Compared to the average values found in the mock catalogues, the constraint on α_\perp is better than expected, whereas the constraint on α_\parallel is slightly worse. For comparison, we show the Data Release 11 constraints from Anderson et al. (2014) along with our new results in Table 8. There is a slight decrease in the constraining power of the new results for the CMASS sample mainly due to the change in the methodology of generating the mock catalogues. Although the fitting results using MD-Patchy mocks are found to be more constraining than those from QPM mocks, we prefer to err on the conservative side and quote the results from QPM mocks. A comparison of the results with both sets of mocks is revisited in Anderson et al. (2016, in preparation).

The significance of the BAO detection, however, has increased from Data Release 11 to Data Release 12. Figure 7 presents the χ^2 surface from the isotropic fitting of the DR12

Table 6. Results of the anisotropic BAO fittings in the QPM mocks of the LOWZ and CMASS samples. We present median values \tilde{x} , scatter S_x , median uncertainties $\tilde{\sigma}_x$, and scatter in the uncertainties S_{σ_x} for α_{\parallel} and α_{\perp} . We also show the median values and scatter for α and ϵ for reference. The variables with a tilde indicate the median of that variable. S denotes the root mean square deviation in that variable.

	$\tilde{\alpha}$	S_{α}	$\tilde{\epsilon}$	S_{ϵ}	$\tilde{\alpha}_{\parallel}$	$S_{\alpha_{\parallel}}$	$\tilde{\sigma}_{\alpha_{\parallel}}$	$S_{\sigma_{\alpha_{\parallel}}}$	$\tilde{\alpha}_{\perp}$	$S_{\alpha_{\perp}}$	$\tilde{\sigma}_{\alpha_{\perp}}$	$S_{\sigma_{\alpha_{\perp}}}$
LOWZ pre-recon	1.0036	0.0337	+0.0021	0.0362	1.0084	0.0874	0.0905	0.0431	1.0012	0.0406	0.0365	0.0161
LOWZ post-recon	1.0017	0.0177	+0.0009	0.0235	1.0057	0.0526	0.0524	0.0363	1.0007	0.0270	0.0248	0.0089
CMASS pre-recon	1.0025	0.0152	+0.0018	0.0196	1.0061	0.0452	0.0482	0.0234	1.0013	0.0217	0.0223	0.0041
CMASS post-recon	1.0019	0.0105	+0.0026	0.0149	1.0067	0.0336	0.0312	0.0168	0.9987	0.0167	0.0156	0.0025

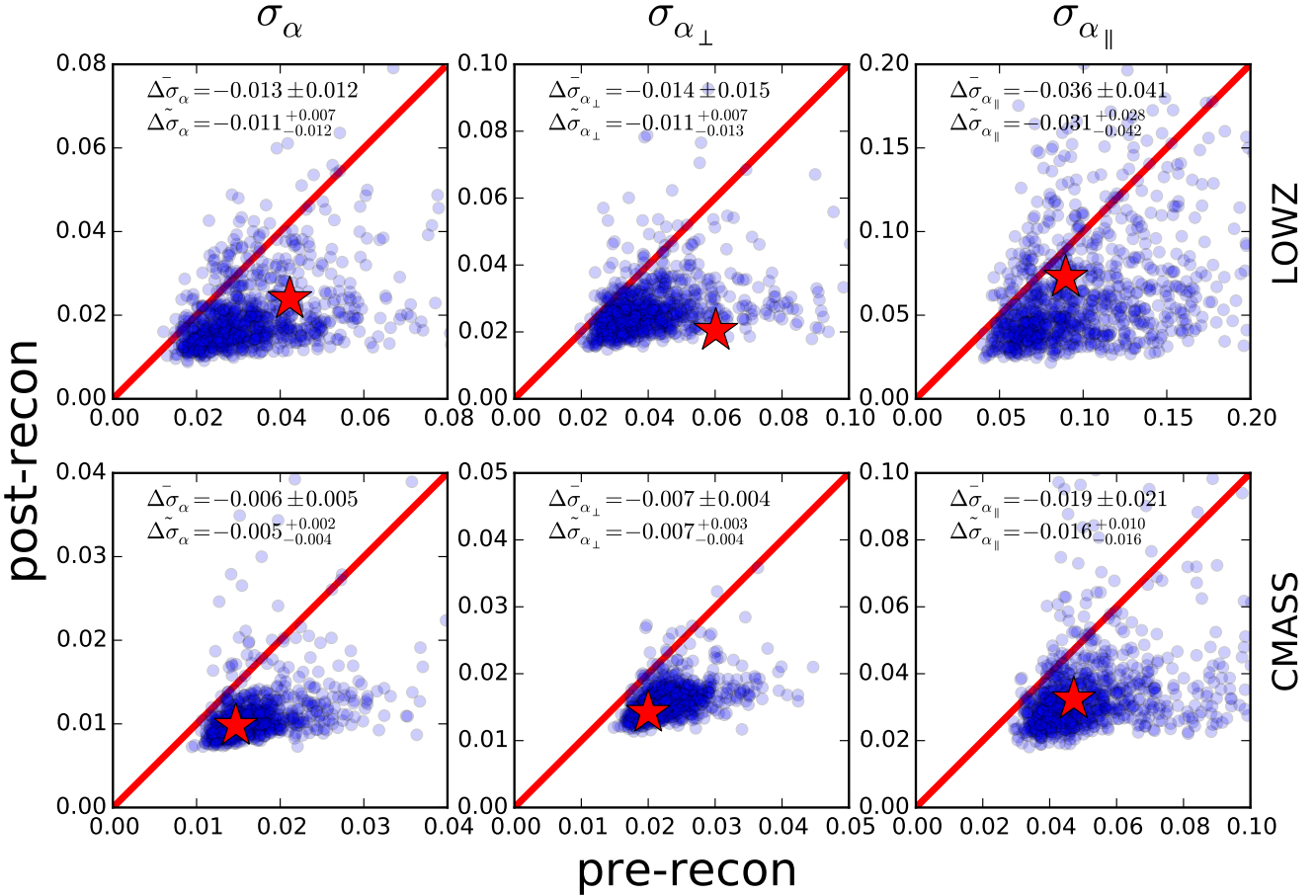


Figure 4. Comparison of the pre- and post-reconstruction uncertainties in the anisotropic BAO fittings in QPM mocks. From left to right, we show how reconstruction generally improves σ_{α} , $\sigma_{\alpha_{\perp}}$ and $\sigma_{\alpha_{\parallel}}$ respectively. The top row presents the results for LOWZ mocks and bottom row shows CMASS mocks. The uncertainties found in the Data Release 12 catalogues are shown with a red star.

correlation functions. Solid lines represent the difference between $\chi^2(\alpha)$ and its value at the best-fit χ^2_{\min} using our de-wiggled template. Dashed lines show the same when trying to fit the data using a template without a BAO peak (Eisenstein & Hu 1998). The red lines correspond to LOWZ galaxies, blue lines correspond to CMASS galaxies. In this figure the position of the BAO peak is detected with $\simeq 10\sigma$ for CMASS and $\gtrsim 5\sigma$ for LOWZ, whereas the presence of BAO in the correlation function is detected at $\simeq 8\sigma$ for

CMASS and $\simeq 4\sigma$ for LOWZ. An apparent decrease in the significance of BAO with increasing α (measured by the difference between the solid and the dashed lines) is seen in this plot. This decrease is caused by our methodology in which the whole de-wiggled template (not just the BAO component) is shifted by α to fit the data, so the ability of our model in equation 2 to reproduce the shape of the correlation function given the different size of the error bars at

Table 7. Results of the anisotropic fittings of the BAO feature in the correlation function of LOWZ and CMASS galaxy samples, before and after reconstruction. We present the measured value and 1σ uncertainties for α and ϵ . Since these two variables are correlated, we include their correlation $\rho_{\alpha\epsilon} = \sigma_{\alpha\epsilon}/\sigma_{\alpha}\sigma_{\epsilon}$. The corresponding values and uncertainties for α_{\parallel} and α_{\perp} , together with their correlation, are displayed as well. The last column shows the minimum value of χ^2 and the number of degrees of freedom in the fit.

	α	ϵ	$\rho_{\alpha\epsilon}$	α_{\parallel}	α_{\perp}	$\rho_{\alpha_{\parallel}\alpha_{\perp}}$	χ^2/dof
LOWZ pre-recon	1.0035 ± 0.0423	$+0.0259 \pm 0.0407$	-0.1302	1.0562 ± 0.0896	0.9782 ± 0.0602	-0.3034	19.2/26
LOWZ post-recon	1.0257 ± 0.0239	$+0.0058 \pm 0.0262$	+0.6770	1.0377 ± 0.0726	1.0197 ± 0.0204	-0.2888	24.6/26
CMASS pre-recon	1.0185 ± 0.0147	-0.0162 ± 0.0197	+0.4127	0.9858 ± 0.0472	1.0352 ± 0.0200	-0.5169	26.1/26
CMASS post-recon	1.0051 ± 0.0098	-0.0305 ± 0.0141	+0.4169	0.9446 ± 0.0324	1.0368 ± 0.0142	-0.5671	25.6/26

Table 8. Comparison of DR11 and DR12 fitting results from the correlation function of LOWZ and CMASS. The value of α from the isotropic fitting is labelled as α_{iso} to distinguish it from the value from the anisotropic fitting. The DR11 results are taken from Table 10 of Anderson et al. (2014) and Table 3 of Tojeiro et al. (2014). They correspond to the ones quoted from the correlation function analysis (for a single bin centre choice and de-wiggled template where available), and have been re-scaled to the fiducial cosmology in this paper.

	Pre-Reconstruction			Post-Reconstruction		
	α_{iso}	α	ϵ	α_{iso}	α	ϵ
LOWZ-DR11	1.006 ± 0.033	-	-	1.002 ± 0.019	-	-
LOWZ-DR12	1.009 ± 0.030	1.004 ± 0.042	$+0.026 \pm 0.041$	1.023 ± 0.017	1.026 ± 0.024	$+0.006 \pm 0.026$
CMASS-DR11	1.025 ± 0.013	1.019 ± 0.014	-0.008 ± 0.018	1.0145 ± 0.0090	1.0106 ± 0.0089	-0.030 ± 0.013
CMASS-DR12	1.015 ± 0.013	1.019 ± 0.015	-0.016 ± 0.020	1.0093 ± 0.0097	1.0051 ± 0.0098	-0.031 ± 0.014

different radial separations results in a residual dependence of χ^2 on α .

4.3 Consensus values from $\xi(s)$ and $P(k)$

This section combines the fitting results from the two-point statistics measuring the clustering in configuration space (i.e. the correlation function, described in this paper) and in Fourier space (i.e. the power spectrum, described in the companion paper Gil-Marín et al. 2016). As in Data Release 11, these are expected to be highly correlated but sensitive to the clustering in different scale ranges. In configuration space we also take into account that the measurement shows some scatter depending on the position of the bin centres, the resulting value is labelled as *combined* $\xi(s)$. The methodology we follow to combine the results from correlation function and power spectrum was described in Section 4.3 of Anderson et al. (2014). A brief summary goes as follows: we compute the correlation coefficient r between $\xi(s)$ and $P(k)$ measurements using the fitting results of the mocks, from which we find a correlation of 0.91 for LOWZ and 0.90 for CMASS. The consensus value is then computed as the average of the α measurements from the DR12 $\xi(s)$ and $P(k)$, with an error bar of $\sigma((1+r)/2)^{1/2}$, where σ is the average of the σ_{α} values from $\xi(s)$ and $P(k)$. We show in Table 9 the median and scatter from $\xi(s)$ and $P(k)$ measurements from QPM mocks, as well as the consensus value that combines both.

We now apply the same methodology to the observations reported in this paper. The fitting results from Data Release 12 CMASS and LOWZ galaxies are shown in Table 10. Since the results are highly correlated, the scatter is only slightly reduced due to the combination of both measurements, with respect to the uncertainty on each individual measurement. The good agreement between the BAO

Table 9. Fitting results of the QPM mocks catalogues for LOWZ and CMASS. Power spectrum values taken from the anisotropic fittings from Gil-Marín et al. (2016) and have been re-scaled to the fiducial cosmology in this paper.

Estimator	$\langle\alpha\rangle$	S_{α}	$\langle\sigma_{\alpha}\rangle$	$\langle\chi^2\rangle / \text{dof}$
QPM LOWZ				
Consensus $P(k) + \xi(s)$	1.00217	0.01569	0.01617	-
combined $\xi(s)$	1.00251	0.01578	0.01624	-
post-recon $P(k)$	1.00185	0.01631	0.01684	-
post-recon $\xi(s)$	1.00253	0.01617	0.01642	15.6/15
pre-recon $\xi(s)$	1.00233	0.02648	0.02750	16.1/15
QPM CMASS				
Consensus $P(k) + \xi(s)$	0.99981	0.00982	0.01010	-
combined $\xi(s)$	1.00216	0.00981	0.01025	-
post-recon $P(k)$	0.99753	0.01034	0.01047	-
post-recon $\xi(s)$	1.00259	0.01016	0.01056	16.0/15
pre-recon $\xi(s)$	1.00304	0.01471	0.01528	16.1/15

fitting analyses in real and Fourier space, being complementary and affected differently by systematic effects, provides a reassuring and robust measurement of the distance scale. In this table we also indicate the consensus results including the systematic error budget we accounted for in Anderson et al. (2014) (labelled as *stat+sys*). This systematic error budget consists of a 0.3 per cent in α for fitting and survey effects, a 0.3 per cent in α for unmodelled astrophysical shifts, and an additional independent systematic error of 0.5 per cent in quadrature to ϵ , as detailed in Section 8.1 of Anderson et al. (2014).

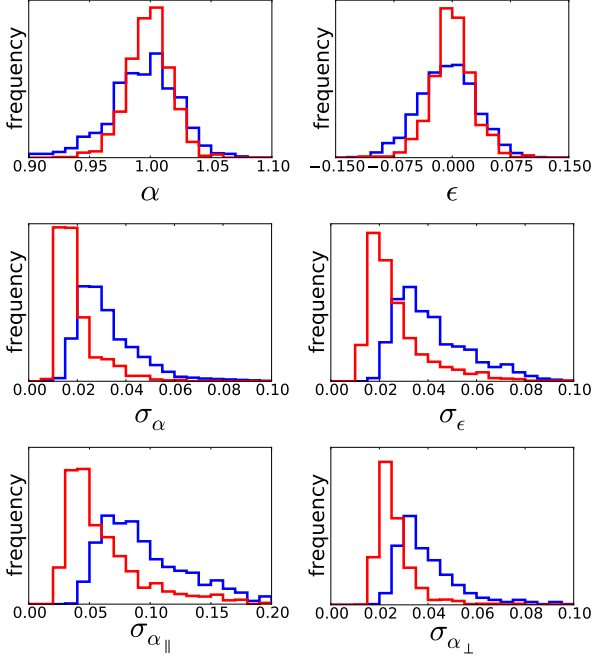


Figure 5. Statistics of BAO anisotropic fittings in LOWZ mocks. We present the distribution of measured values of α and ϵ in the mocks (top panels), as well as of their uncertainties σ_α and σ_ϵ (middle panels). Bottom panels show the distribution of the uncertainties in the line of sight distance scale and in the perpendicular direction $\sigma_{\alpha_\parallel}$ and σ_{α_\perp} respectively. Blue lines represent the pre-reconstruction BAO fittings, red lines display the post-reconstruction ones.

Table 10. Results of the fittings of the DR12 data. Power spectrum fittings from Gil-Marín et al. (2016) and have been re-scaled to the fiducial cosmology in this paper.

Estimator	α	χ^2/dof
DR12 LOWZ		
Consensus $P(k) + \xi(s)$ (stat+syst)	1.0370 ± 0.0177	-
Consensus $P(k) + \xi(s)$	1.0370 ± 0.0172	-
combined $\xi(s)$	1.0251 ± 0.0169	-
post-recon $P(k)$	1.0489 ± 0.0183	56/43
post-recon $\xi(s)$	1.0230 ± 0.0170	9/15
pre-recon $P(k)$	1.0061 ± 0.0306	36/43
pre-recon $\xi(s)$	1.0085 ± 0.0300	13/15
DR12 CMASS		
Consensus $P(k) + \xi(s)$ (stat+syst)	1.0047 ± 0.0099	-
Consensus $P(k) + \xi(s)$	1.0047 ± 0.0090	-
combined $\xi(s)$	1.0064 ± 0.0096	-
post-recon $P(k)$	1.0029 ± 0.0088	37/38
post-recon $\xi(s)$	1.0093 ± 0.0097	26/15
pre-recon $P(k)$	1.0101 ± 0.0152	38/38
pre-recon $\xi(s)$	1.0153 ± 0.0134	12/15

4.4 Summary of the fitting results

From the isotropic fittings of the CMASS correlation function, and after accounting for systematic errors, we infer that $D_V(z = 0.57)/r_d = 13.87 \pm 0.19$ (pre-reconstruction) and 13.79 ± 0.14 (post-reconstruction). Combining with post-reconstruction $P(k)$ BAO fittings, a consensus value of

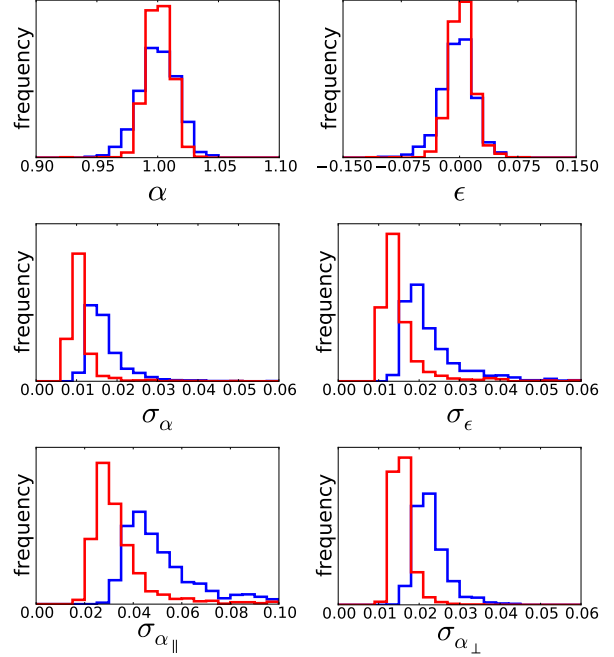


Figure 6. Statistics of BAO anisotropic fittings in CMASS mocks. We present the distribution of measured values of α and ϵ in the mocks (top panels), as well as of their uncertainties σ_α and σ_ϵ (middle panels). Bottom panels show the distribution of the uncertainties in the line of sight distance scale and in the perpendicular direction $\sigma_{\alpha_\parallel}$ and σ_{α_\perp} respectively. Blue lines represent the pre-reconstruction BAO fittings, red lines display the post-reconstruction ones.

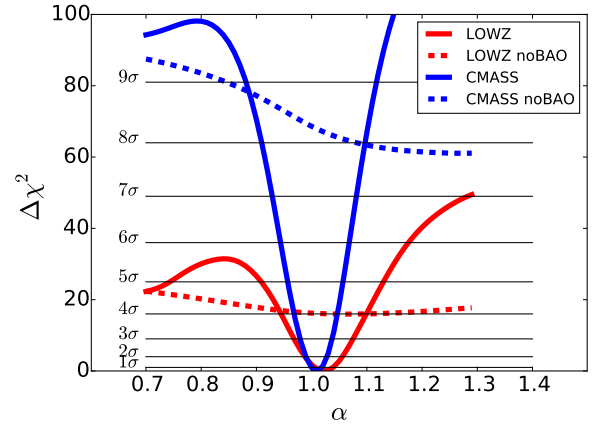


Figure 7. Likelihood surfaces $\chi^2(\alpha)$ from the isotropic fitting of the DR12 data post-reconstruction. The results for LOWZ are shown in red and for CMASS are presented in blue. Solid lines correspond to the fitting of the monopole of the correlation function to a template that includes BAO, dashed lines show the case in which the BAO feature in the template has been smoothed away. All lines have been subtracted the χ^2 value at the minimum when the template with BAO is used. For reference, we note the significance of the detection of the BAO with horizontal lines.

$D_V(z = 0.57)/r_d = 13.73 \pm 0.14$ is obtained, slightly less constraining than the DR11 measurement of 13.77 ± 0.13 . From the isotropic fittings of the LOWZ correlation function we infer that $D_V(z = 0.32)/r_d = 8.47 \pm 0.25$ (pre-reconstruction) and 8.59 ± 0.15 (post-reconstruction). The combination of the latter with the fitting of BAO in the power spectrum post-reconstruction returns a consensus value of $D_V(z = 0.32)/r_d = 8.71 \pm 0.15$ which improves the DR11 measurement of 8.47 ± 0.17 . The difference between $P(k)$ and $\xi(s)$ measurements is slightly larger in LOWZ than in CMASS, which might explain the difference with the DR11 value despite the small increase in the sampled volume. The post-reconstruction value for the correlation function will be used in our MCMC chains when the isotropic BAO results are included. If the anisotropic BAO results are used instead, then we use the two-dimensional likelihood surface $P(D_A, H) \propto \exp(-0.5\chi^2(D_A, H))$ from the anisotropic fitting without any Gaussian approximation.

We summarize the distance constraints from the anisotropic BAO analysis of the correlation function of the CMASS and LOWZ samples from the Data Release 12 of the Baryon Oscillation Spectroscopic Survey in Table 11. Post-reconstruction, our measurements imply a 1.5 per cent determination of $D_A(z = 0.57)$ and a 2.0 per cent measurement of $D_A(z = 0.32)$, determining the expansion rate $H(z)$ with a precision of 3.7 per cent at $z = 0.57$ and 7.1 per cent at $z = 0.32$. The isotropic fittings produce a 1.0 per cent measurement of the distance to redshift $z = 0.57$ and a 1.7 per cent determination of the distance to $z = 0.32$. All the uncertainties quoted assume that the sound horizon scale is known to within a much better precision and therefore its contribution to the error budget is negligible, which is the case in Λ CDM and the models studied in Section 5, but not necessarily in more general cosmological models. In that case, the uncertainties above would be valid for the quantities $D_A(z)/r_d$ and $H(z)r_d$, but not for $D_A(z)$ and $H(z)$.

Figure 8 compares the distance constraints from the post-reconstruction isotropic and the anisotropic analysis. Contours represent the anisotropic fitting of CMASS and LOWZ and dashed lines the isotropic fitting. In both cases we show the 1-sigma and 2-sigma constraints. The faint contours in the left panel show the DR11 CMASS constraints for comparison. We also include, for reference, the constraints from a Planck 2015 Λ CDM model (Planck Collaboration et al. 2015b) colour-coded according to the corresponding value of the Hubble constant (colour points). We note that the DR12 CMASS contours have shifted slightly upwards compared to DR11, favouring larger values of $H(z = 0.57)r_d/r_d^{\text{fid}}$. However, this change is not large enough to make our measurement inconsistent with the Λ CDM model prediction from Planck 2015.

5 COSMOLOGICAL INTERPRETATION

In this section we infer the constraints from the BOSS Data Release 12 BAO measurements on the cosmological parameters from different cosmological models. We use the Markov Chain Monte Carlo (MCMC) code CosmoMC⁷ (Lewis &

Bridle 2002) to compute our cosmological constraints. Our goal in this section is double. First, we present a comparison with the results in Anderson et al. (2014) with the same cosmological datasets except for the DR12 BAO measurements reported in this paper, addressing the improvement from our updated BAO measurements on constraining the cosmological parameters. Second, we want to take advantage of more powerful cosmological datasets not available at the time of Anderson et al. (2014) to obtain updated cosmological constraints that can be compared with current literature, such as Planck Collaboration et al. (2015b).

We begin with a comparison to the results in Anderson et al. (2014). Here we combine our BAO measurements with Cosmic Microwave Background (CMB) data from Planck+WP (Planck Collaboration et al. 2014), which hereafter we refer to as Planck13, or simply as *Planck*. The current CMB measurements from the Planck satellite (Planck Collaboration et al. 2015a) are referred to as Planck15. Figure 9 displays the cosmological constraints from Planck13 and our Data Release 12 BAO constraints (blue contours) compared to those from the same CMB data combined with Data Release 11 BAO (red contours). The results are shown for the different cosmological models studied here: flat Universe (left panels) where dark energy is described by a cosmological constant (Λ CDM, top panel), dark energy with constant but arbitrary equation of state (w CDM, middle panel), and with a time-dependent equation of state (w_0w_a CDM, bottom panel). Also shown are their non-flat versions where curvature is a free parameter (right panels: $o\Lambda$ CDM, ow CDM, ow_0w_a CDM respectively). The following priors are assumed: $-0.1 < \Omega_k < +0.1$, $-3 < w_0 < +1$, and $-3 < w_a < +3$. As readily seen in this plot, the change from DR11 is incremental. Furthermore, we have checked that the small decrease in the size of these contours is mostly driven by the smaller error bar in the DR12 LOWZ distance constraint.

A full compilation of our cosmological results is presented in Table 12. In these MCMC chains, when we include the Type-1a Supernovae data we use the Union 2 compilation by the Supernovae Cosmology Project (Suzuki et al. 2012) for direct comparison with Anderson et al. (2014). We include the low-redshift BAO measurement from the 6-degree field galaxy redshift survey (6DF) (Beutler et al. 2011), and the Lyman- α BAO measurements from Delubac et al. (2015) and Font-Ribera et al. (2014a)⁸.

This table reveals that the combination of CMB+BAO+SN greatly improves the constraints on curvature and dark energy. There is an improvement in the Figure of Merit of dark energy (Albrecht et al. 2006) of 10 per cent with respect to our CMB+BAO+SN results from Data release 11 and a 50 per cent improvement if the SN sample is replaced by the recent JLA compilation from Betoule et al. (2014).

Now we study the constraints from the BAO in CMASS and LOWZ combined with the recent Planck15 temperature plus polarization power spectrum (Planck Collaboration et al. 2015c); these results are shown in Table 13. In or-

⁸ For Data Release 11, an extensive study of the cosmological consequences of Galaxy and Lyman- α BAO from BOSS was presented in Aubourg et al. (2015).

⁷ <http://cosmologist.info/cosmomc>

Table 11. Distance constraints from the analysis of the BAO in the correlation function of CMASS and LOWZ samples. We quote our results on the angle-averaged distance $D_V(z)$, the angular diameter distance $D_A(z)$, the Hubble parameter $H(z)$, and the correlation $\rho_{D_A, H}$ between $D_A(z)$ and $H(z)$. A fiducial sound horizon value of $r_d^{\text{fid}} = 147.10$ Mpc is assumed. The distance constraints are quoted at redshift $z = 0.57$ for the CMASS sample and $z = 0.32$ for the LOWZ sample. The error bars in these constraints include the contribution from the systematic error budget.

Sample	$D_V(z)r_d^{\text{fid}}/r_d$ (Mpc)	$D_A(z)r_d^{\text{fid}}/r_d$ (Mpc)	$H(z)r_d/r_d^{\text{fid}}$ ($\text{km s}^{-1}\text{Mpc}^{-1}$)	$\rho_{D_A, H}$
LOWZ Pre-Recon	1246 ± 37	941 ± 58	77.8 ± 6.6	0.31
LOWZ Post-Recon	1264 ± 22	981 ± 20	79.2 ± 5.6	0.29
CMASS Pre-Recon	2040 ± 28	1399 ± 28	96.1 ± 4.8	0.51
CMASS Post-Recon	2028 ± 21	1401 ± 21	100.3 ± 3.7	0.55

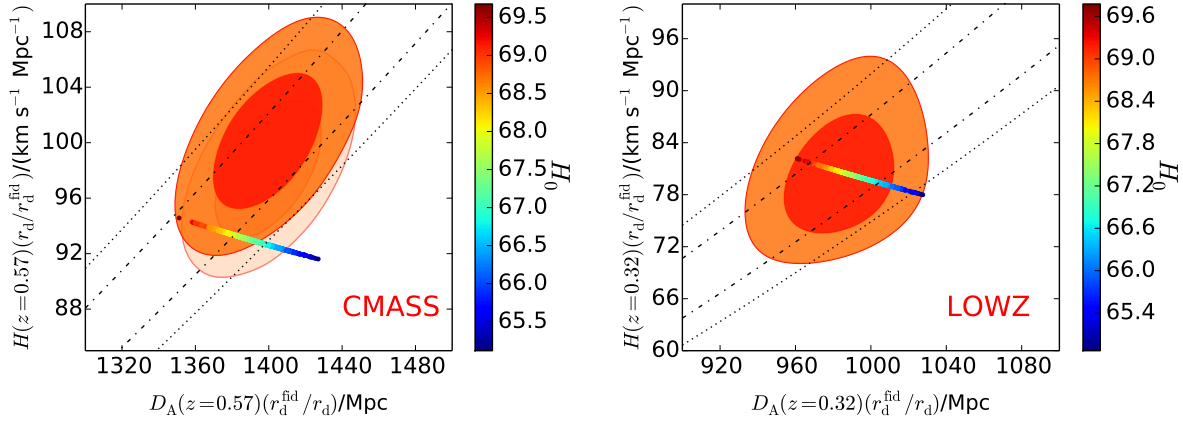


Figure 8. Left panel: Anisotropic (solid contours) and isotropic (dashed and dotted lines) constraints for $D_A(z = 0.57)/r_d$ and $H(z = 0.57)r_d$ from CMASS-DR12 from the analysis using QPM mocks. Light-shaded contours show the constraints from CMASS-DR11 for comparison. Right panel: constraints on $D_A(z = 0.32)/r_d$ and $H(z = 0.32)r_d$ from the isotropic and anisotropic fitting of LOWZ-DR12 also using QPM mocks. In both cases 1σ and 2σ contours are shown. Also included is a small region colour-coded according to the value of the Hubble constant from the constraints from Planck 2015 temperature and polarization power spectrum data assuming a Λ CDM model.

der to present the most up-to-date results we also replace the Union 2 Supernovae sample with the more recent JLA compilation (Betoule et al. 2014). The low-redshift BAO measurement of 6DF here is combined with that from the SDSS Main Galaxy Sample (MGS) sample (Ross et al. 2015).

Since the results in Table 13 are more constraining, we will focus on them. The Λ CDM constraint on the Hubble constant has an error bar nearly half its size for the CMB only case in Planck Collaboration et al. (2015b), creating tension for any reported values of H_0 larger than $70 \text{ km s}^{-1} \text{ Mpc}^{-1}$. This result follows the recent analyses of *inverse distance ladder* measurements of Aubourg et al. (2015); Heavens, Jimenez & Verde (2014); Cuesta et al. (2015). The Λ CDM cosmology is completely consistent with the fiducial cosmology adopted in Anderson et al. (2016, in preparation). The curvature is also reported here with an error bar half its size in Planck Collaboration et al. (2015b) for the CMB+BAO+JLA+ H_0 dataset combination ($\Omega_K = 0.0008 \pm 0.0040$) and is consistent with flatness. The equation of state of dark energy is also reported with an error bar half its size in Planck Collaboration et al. (2015b) for the CMB+BAO+JLA+ H_0 dataset combination ($w = -1.02 \pm 0.08$) and is consistent with a cosmological constant. The figure of merit from the combi-

nation Planck13+DR11+Union2 increases by a factor of 1.8 when using Planck15+DR12+JLA (see Figure 10).

Finally, if one is interested in combining the updated results from CMASS with the WiggleZ (Blake et al. 2011; Kazin et al. 2014) results, one can use the correlation matrix in Beutler et al. (2016), updated to the actual effective volume in CMASS Data Release 12:

$$\tilde{R} = \begin{pmatrix} 1 & & & \\ 0.039 & 1 & & \\ 0.020 & 0.57 & 1 & \\ 0.014 & 0.39 & 0.51 & 1 \end{pmatrix} \quad (7)$$

and build the covariance matrix $\tilde{C} = V^T \tilde{R} V$ with $V = (21, 65, 200, 86)$ Mpc. This covariance matrix contains the errors and covariances of the angle-averaged distance measurements from CMASS, the CMASS-WiggleZ cross-correlation, WiggleZ, and the high redshift WiggleZ samples. The corresponding data vector would be $D = (2028, 2132, 2100, 2516)$ Mpc. Although we do not use this in our cosmological constraints, we find it useful since in those cases where the anisotropic constraints from CMASS are not much better than the isotropic ones (see Table 12), one can benefit from the extra amount of information from WiggleZ BAO measurements and their cross-correlation with CMASS.

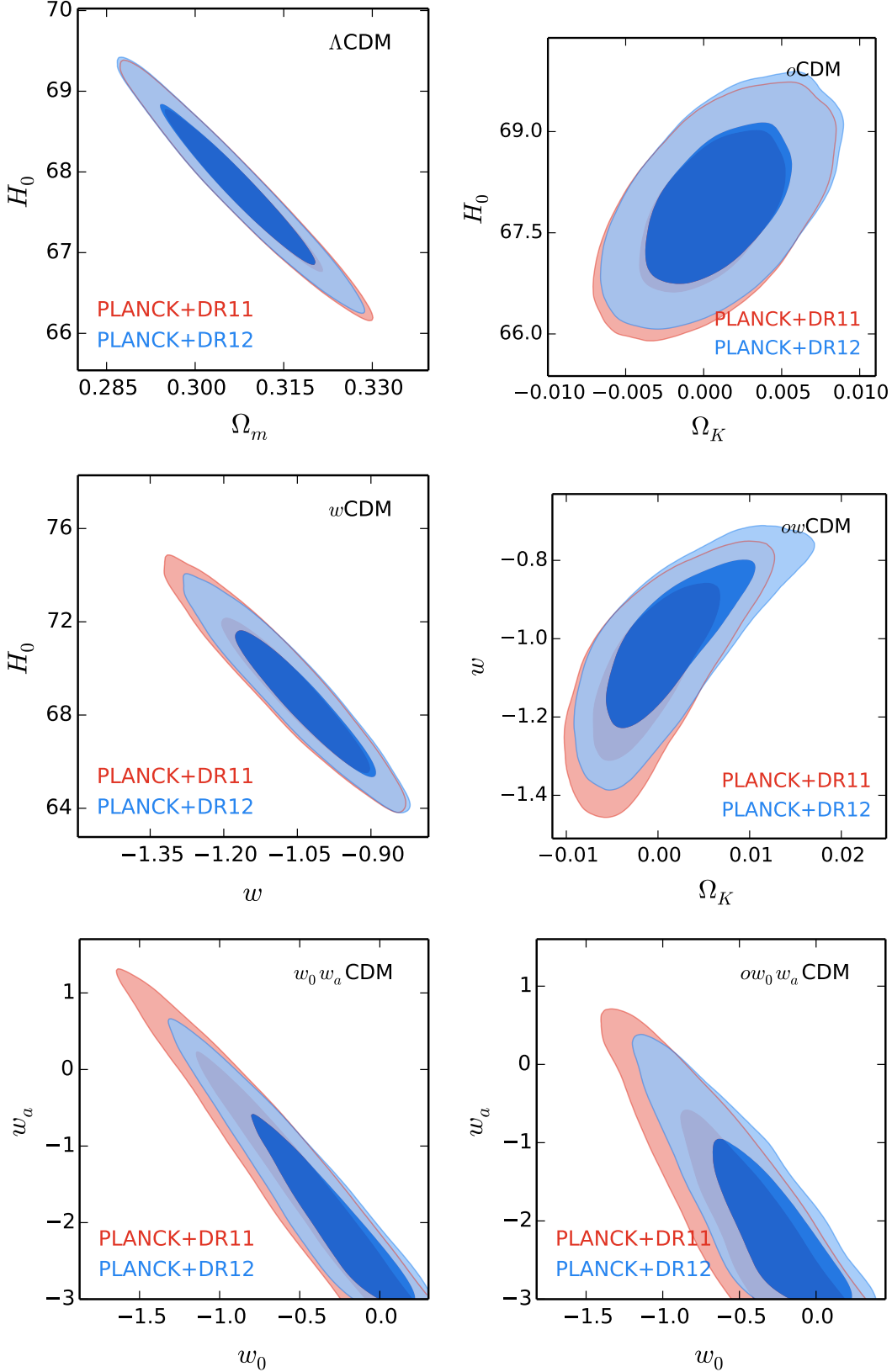


Figure 9. Cosmological constraints for different cosmological models, using a combination of Planck13 CMB data and our DR12 BAO measurements (blue contours). Also shown for comparison are the constraints from Anderson et al. (2014) where the DR11 BAO measurements are used instead (red contours). Left panels assume a flat Universe: Λ CDM (top panel), w CDM (middle panel), and $w_0 w_a$ CDM (bottom panel). On the right panels the curvature is a free parameter: o CDM (top panel), ow CDM (middle panel), and $ow_0 w_a$ CDM (bottom panel). The following priors are assumed: $-0.1 < \Omega_k < +0.1$, $-3 < w_0 < +1$, and $-3 < w_a < +3$.

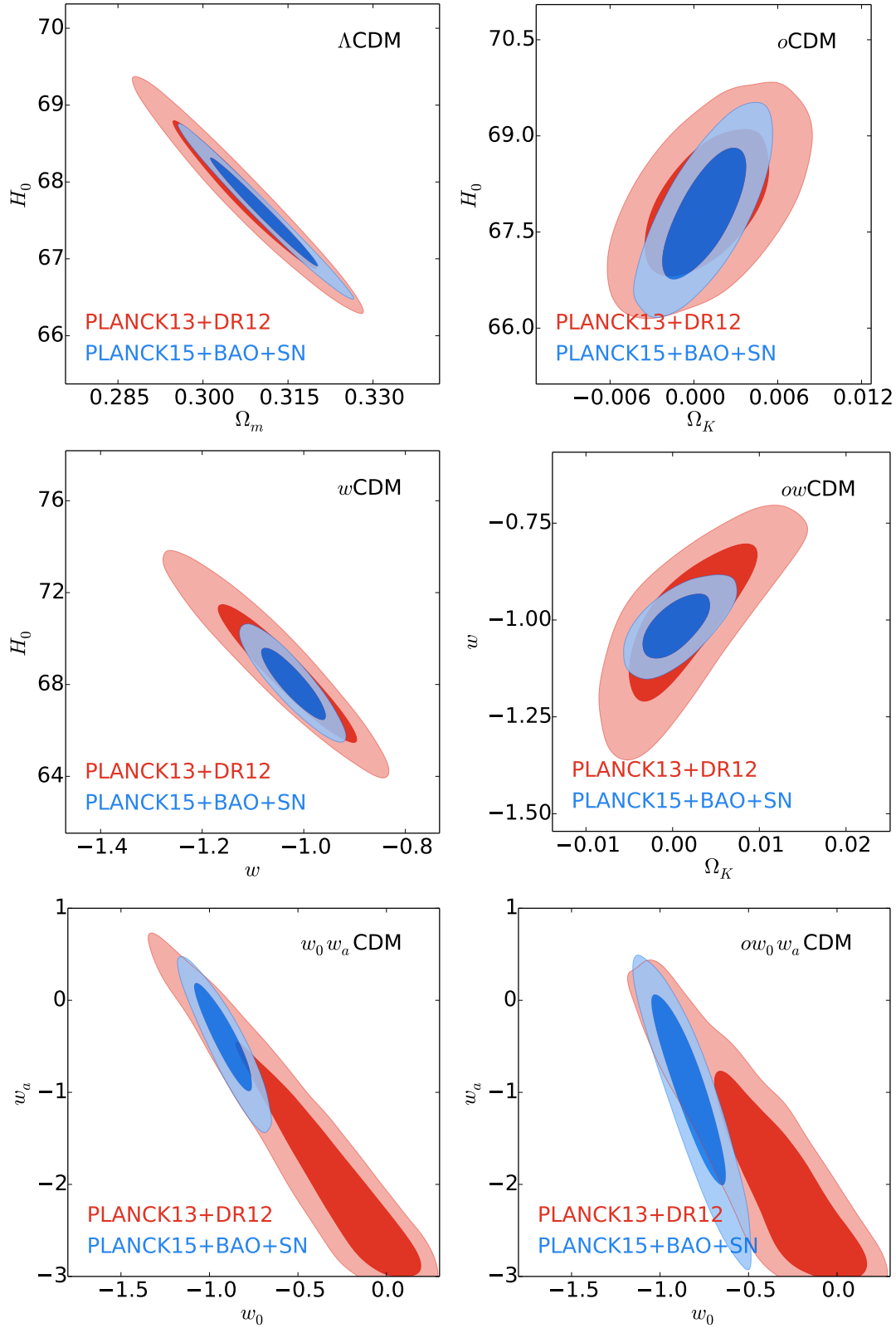


Figure 10. Cosmological constraints for different cosmological models, using a combination of Planck15 TT+TE+EE power spectra, JLA SN data, and our DR12 BAO measurements (blue contours). Also shown for comparison are the constraints from Figure 9 where no supernovae data is used and Planck15 CMB data is replaced with Planck13 (red contours). The left panels assume a flat Universe: Λ CDM (top panel), w CDM (middle panel), and w_0w_a CDM (bottom panel). In the right panels the curvature is a free parameter: o CDM (top panel), ow CDM (middle panel), and ow_0w_a CDM (bottom panel). The following priors are assumed: $-0.1 < \Omega_k < +0.1$, $-3 < w_0 < +1$, and $-3 < w_a < +3$.

Table 12. Cosmological constraints by different dataset combinations in the cosmological models Λ CDM, oCDM , w CDM, owCDM , w_0w_a CDM, and ow_0w_a CDM. For direct comparison to Table 15 in Anderson et al. (2014), we compare the cosmological constraints from combining Planck13 with distance scale measurements from BOSS DR12 galaxies as well as lower and higher redshift BAO measurements from the 6-degree field galaxy redshift survey (6DF) and the BOSS-Lyman alpha forest (Ly α F), respectively. We also compare how these combinations benefit from the constraining power of type-Ia Supernovae from the Union 2 compilation by the Supernovae Cosmology Project (SN). The WMAP and eWMAP cases have been added for comparison. 'CMASS-iso' indicates the isotropic measurement from the CMASS sample, whereas the anisotropic one is referred to simply as 'CMASS'. 'LOWZ' is the isotropic measurement from the LOWZ sample. 'BAO' stands for the combination CMASS + LOWZ + 6DF + Ly α F. Numbers in parenthesis represent the uncertainty in the accompanying value, e.g. 0.123 (45) should be read as 0.123 ± 0.045 .

Cosmological Model	Data Sets	$\Omega_m h^2$	Ω_m	H_0 km s $^{-1}$ Mpc $^{-1}$	Ω_K	w_0	w_a
Λ CDM	Planck + CMASS-iso + LOWZ	0.1413 (14)	0.307 (8)	67.9 (6)			
Λ CDM	Planck + CMASS + LOWZ	0.1413 (13)	0.307 (8)	67.8 (6)			
Λ CDM	Planck + BAO	0.1416 (13)	0.309 (8)	67.7 (6)			
Λ CDM	Planck + CMASS + LOWZ + SN	0.1412 (13)	0.307 (8)	67.9 (6)			
Λ CDM	Planck + BAO + SN	0.1415 (13)	0.308 (7)	67.7 (5)			
Λ CDM	WMAP + BAO + SN	0.1398 (22)	0.301 (8)	68.2 (7)			
Λ CDM	eWMAP + BAO + SN	0.1409 (16)	0.300 (8)	68.5 (6)			
oCDM	Planck + CMASS-iso + LOWZ	0.1418 (25)	0.307 (8)	68.0 (8)	+0.0008 (30)		
oCDM	Planck + CMASS + LOWZ	0.1421 (25)	0.308 (8)	67.9 (7)	+0.0010 (30)		
oCDM	Planck + BAO	0.1424 (25)	0.310 (8)	67.8 (7)	+0.0010 (29)		
oCDM	Planck + CMASS + LOWZ + SN	0.1418 (24)	0.307 (8)	68.0 (7)	+0.0008 (29)		
oCDM	Planck + BAO + SN	0.1420 (24)	0.308 (7)	67.9 (7)	+0.0008 (29)		
oCDM	WMAP + BAO + SN	0.1387 (41)	0.299 (9)	68.1 (7)	-0.0015 (40)		
oCDM	eWMAP + BAO + SN	0.1367 (34)	0.296 (8)	68.0 (7)	-0.0050 (35)		
w CDM	Planck + CMASS-iso + LOWZ	0.1429 (22)	0.290 (19)	70.3 (26)		-1.11 (11)	
w CDM	Planck + CMASS + LOWZ	0.1420 (21)	0.301 (15)	68.7 (20)		-1.04 (9)	
w CDM	Planck + BAO	0.1415 (21)	0.309 (13)	67.7 (17)		-1.00 (7)	
w CDM	Planck + CMASS + LOWZ + SN	0.1422 (19)	0.300 (12)	68.9 (15)		-1.05 (7)	
w CDM	Planck + BAO + SN	0.1419 (19)	0.305 (11)	68.2 (14)		-1.02 (6)	
w CDM	WMAP + BAO + SN	0.1371 (35)	0.308 (11)	66.7 (16)		-0.92 (8)	
w CDM	eWMAP + BAO + SN	0.1372 (28)	0.313 (11)	66.3 (15)		-0.88 (7)	
owCDM	Planck + CMASS-iso + LOWZ	0.1419 (24)	0.282 (28)	71.3 (36)	-0.0019 (40)	-1.17 (18)	
owCDM	Planck + CMASS + LOWZ	0.1422 (25)	0.307 (22)	68.2 (24)	+0.0016 (49)	-1.01 (13)	
owCDM	Planck + BAO	0.1423 (25)	0.320 (18)	66.8 (18)	+0.0034 (46)	-0.94 (10)	
owCDM	Planck + CMASS + LOWZ + SN	0.1421 (25)	0.301 (14)	68.8 (16)	+0.0001 (35)	-1.05 (8)	
owCDM	Planck + BAO + SN	0.1423 (25)	0.308 (13)	68.0 (14)	+0.0010 (34)	-1.01 (7)	
owCDM	WMAP + BAO + SN	0.1372 (43)	0.308 (13)	66.7 (16)	+0.0000 (46)	-0.92 (8)	
owCDM	eWMAP + BAO + SN	0.1356 (35)	0.308 (13)	66.4 (14)	-0.0028 (42)	-0.91 (7)	
w_0w_a CDM	Planck + CMASS-iso + LOWZ	0.1431 (22)	0.333 (48)	66.2 (52)		-0.68 (46)	-1.13 (114)
w_0w_a CDM	Planck + CMASS + LOWZ	0.1425 (21)	0.370 (37)	62.3 (34)		-0.34 (34)	-1.83 (86)
w_0w_a CDM	Planck + BAO	0.1423 (20)	0.373 (29)	61.9 (26)		-0.31 (28)	-1.90 (75)
w_0w_a CDM	Planck + CMASS + LOWZ + SN	0.1430 (22)	0.307 (17)	68.3 (19)		-0.94 (19)	-0.42 (63)
w_0w_a CDM	Planck + BAO + SN	0.1428 (22)	0.314 (16)	67.5 (17)		-0.89 (18)	-0.48 (61)
w_0w_a CDM	WMAP + BAO + SN	0.1367 (42)	0.304 (16)	67.1 (17)		-0.97 (16)	0.12 (56)
w_0w_a CDM	eWMAP + BAO + SN	0.1363 (31)	0.303 (15)	67.2 (17)		-1.00 (15)	0.33 (41)
ow_0w_a CDM	Planck + CMASS-iso + LOWZ	0.1419 (25)	0.326 (46)	66.5 (50)	-0.0043 (45)	-0.65 (41)	-1.61 (104)
ow_0w_a CDM	Planck + CMASS + LOWZ	0.1417 (24)	0.368 (37)	62.3 (33)	-0.0017 (52)	-0.33 (31)	-1.97 (80)
ow_0w_a CDM	Planck + BAO	0.1420 (24)	0.374 (29)	61.7 (25)	-0.0003 (49)	-0.29 (26)	-1.94 (75)
ow_0w_a CDM	Planck + CMASS + LOWZ + SN	0.1420 (25)	0.309 (17)	67.9 (18)	-0.0030 (45)	-0.86 (20)	-0.85 (86)
ow_0w_a CDM	Planck + BAO + SN	0.1422 (25)	0.315 (16)	67.3 (17)	-0.0013 (43)	-0.86 (19)	-0.66 (78)
ow_0w_a CDM	WMAP + BAO + SN	0.1368 (44)	0.304 (16)	67.2 (18)	+0.0033 (71)	-0.99 (17)	0.27 (68)
ow_0w_a CDM	eWMAP + BAO + SN	0.1357 (35)	0.304 (15)	66.9 (17)	-0.0012 (56)	-0.97 (16)	0.18 (56)

6 CONCLUSIONS

In this paper we have measured the position of the baryon acoustic peak in the monopole and quadrupole of the correlation function of the CMASS and LOWZ samples from the Data Release 12 of the Baryon Oscillation Spectroscopic Survey (BOSS). The BAO peak has been detected with high

significance in both samples, representing the best detection of baryon acoustic oscillations ever done by any galaxy survey so far. Using a large set of QPM mock catalogues that reproduce the clustering of the data catalogues we have tested our fitting methodology, which we find unbiased. From the CMASS sample we have measured the distance

Table 13. Cosmological constraints from Planck15+LOWZ+CMASS and from Planck15+LOWZ+CMASS+MGS+6DF+JLA. ‘CMASS’ indicates the anisotropic measurement from the CMASS sample, whereas ‘LOWZ’ is the isotropic measurement from the LOWZ sample. ‘BAO’ stands for the combination LOWZ + CMASS + MGS + 6DF. Numbers in parenthesis represent the uncertainty in the accompanying value, e.g. 0.123 (45) should be read as 0.123 ± 0.045 .

Cosmological Model	Data Sets	$\Omega_m h^2$	Ω_m	H_0 km s ⁻¹ Mpc ⁻¹	Ω_K	w_0	w_a
Λ CDM	Planck15 + LOWZ + CMASS	0.1418 (9)	0.310 (6)	67.7 (4)			
Λ CDM	Planck15 + BAO + SN	0.1420 (9)	0.311 (6)	67.6 (4)			
Λ CDM	Planck15 + LOWZ + CMASS	0.1424 (13)	0.308 (6)	68.0 (6)	+0.0012 (19)		
Λ CDM	Planck15 + BAO + SN	0.1424 (13)	0.310 (6)	67.8 (6)	+0.0008 (20)		
w CDM	Planck15 + LOWZ + CMASS	0.1426 (12)	0.298 (14)	69.2 (17)		-1.06 (7)	
w CDM	Planck15 + BAO + SN	0.1424 (11)	0.307 (9)	68.1 (10)		-1.02 (4)	
ow CDM	Planck15 + LOWZ + CMASS	0.1425 (14)	0.297 (21)	69.4 (26)	+0.0000 (37)	-1.08 (13)	
ow CDM	Planck15 + BAO + SN	0.1424 (13)	0.308 (9)	68.0 (10)	+0.0004 (26)	-1.01 (5)	
$w_0 w_a$ CDM	Planck15 + LOWZ + CMASS	0.1427 (13)	0.370 (36)	62.4 (32)		-0.33 (33)	-1.88 (83)
$w_0 w_a$ CDM	Planck15 + BAO + SN	0.1429 (13)	0.311 (10)	67.8 (10)		-0.91 (10)	-0.44 (39)
$ow_0 w_a$ CDM	Planck15 + LOWZ + CMASS	0.1422 (14)	0.364 (36)	62.8 (32)	-0.0023 (40)	-0.35 (30)	-2.04 (76)
$ow_0 w_a$ CDM	Planck15 + BAO + SN	0.1423 (14)	0.313 (10)	67.5 (11)	-0.0038 (35)	-0.83 (13)	-1.02 (68)

scale to $z = 0.57$ as $D_V(z)r_d^{\text{fid}}/r_d = 2028 \pm 21$ Mpc, where $r_d^{\text{fid}} = 147.10$ Mpc. The LOWZ sample measures the distance to $z = 0.32$ as 1264 ± 22 Mpc. We have also performed the anisotropic fitting of the CMASS correlation function, and for the first time, of the LOWZ correlation function. From this analysis we find an angular diameter distance to $z = 0.57$ of $D_A(z)r_d^{\text{fid}}/r_d = 1401 \pm 21$ Mpc and a distance to $z = 0.32$ of 981 ± 20 Mpc. We also find a Hubble parameter at $z = 0.57$ of $H(z)r_d/r_d^{\text{fid}} = 100.3 \pm 3.7$ km s⁻¹ Mpc⁻¹ and a value at $z = 0.32$ of 79.2 ± 5.6 km s⁻¹ Mpc⁻¹. These values show an excellent agreement with a Λ CDM model with cosmological parameters given by the recent *Planck* 2015 results.

These constraints on the distance scale to $z = 0.32$ and $z = 0.57$ are similar to those in Data Release 11 due to the marginal difference in volume, although a small improvement is seen in LOWZ measurements. Nevertheless, these results can be considered more robust than in DR11 thanks to the improved set of mock catalogues using a novel methodology, and also due to an updated systematics weighting scheme. We realize that the predictions on the precision of the cosmic distance scale measurements made at the beginning of the BOSS survey have been partially met. The forecasted measurement precision for angular diameter distance $D_A(z)$ was 1.0 per cent, 1.0 per cent, and 1.5 per cent at $z = 0.35, 0.6,$ and $2.5,$ respectively, and the forecast precision for the Hubble parameter $H(z)$ was 1.8 per cent, 1.7 per cent, and 1.2 per cent at the same redshifts (Schlegel, White & Eisenstein 2009). Here we report a 1.5 per cent and 2.0 per cent measurement for $D_A(z)$ at $z = 0.57$ and $0.32,$ and a 3.7 per cent and 7.1 per cent measurement for $H(z)$ at the same redshifts, respectively. It remains to be studied whether the discrepancy between the forecasted uncertainties and the measured ones (especially in $H(z)$) is due to a missing ingredient not included in the forecasts (in which case the future is bright for upcoming surveys to reduce the statistical errors), or on the contrary that the measurement is limited by systematics, in which case a larger survey cov-

ering our redshift range might not actually help. Whatever the case may be, the values presented in this paper should be considered as an update of those reported in Anderson et al. (2014), and the final measurements from the BOSS survey will be reported in Anderson et al. (2016, in preparation), in which the CMASS and LOWZ samples from Data Release 12 are combined into a single galaxy catalogue that includes additional galaxies that have traditionally been excluded from the LOWZ sample (Reid et al. 2016, companion paper) but will be recovered in that analysis.

The cosmological constraints reported in this paper have largely benefited from updated cosmological datasets such as the Type-1a Supernovae compilation in Betoule et al. (2014) and the CMB polarization measured by the *Planck* satellite (Planck Collaboration et al. 2015a). We find an improvement of the dark energy Figure of Merit of a factor of 1.8 with respect to Anderson et al. (2014). Moreover we find that the flat Λ CDM model is an excellent fitting to the combination of CMB, BAO, and SN datasets. The values we derive for the cosmological parameters include a curvature parameter of $\Omega_k = +0.0008 \pm 0.0020,$ consistent with a flat geometry of the Universe, and the equation of state of dark energy being $w = -1.02 \pm 0.04,$ completely consistent with a cosmological constant. In the Λ CDM model, the Hubble parameter is found to be $H_0 = 67.6 \pm 0.4$ km s⁻¹ Mpc⁻¹, which does not alleviate the tension with direct measurements of the expansion rate, assuming that the sound horizon scale is known with the precision claimed by *Planck* for this cosmological model.

Having reached the milestone of the 1 per cent precision on the distance scale using BAO, which was already achieved by the BOSS survey since Data Release 11, the future of BAO measurements is promising. Improvements are expected in the next few years extending to higher redshifts with the extended BOSS survey (Dawson et al. 2015) and HETDEX (Hill et al. 2008). Substantial improvements are not expected until results are available from the next generation of experiments, including EUCLID (Laureijs 2009;

Laureijs et al. 2011), LSST (LSST Dark Energy Science Collaboration 2012), SKA (Bull et al. 2015), WFIRST (Spergel et al. 2013a,b), and DESI (Mostek et al. 2012; Levi et al. 2013). It is undeniable, however, that the legacy of BOSS will provide an invaluable guide to analyse and interpret these surveys.

7 ACKNOWLEDGEMENTS

AJC and LV are supported by supported by the European Research Council under the European Community's Seventh Framework Programme FP7-IDEAS-Phys.LSS 240117. Funding for this work was partially provided by the Spanish MINECO under projects AYA2014-58747-P and MDM-2014-0369 of ICCUB (Unidad de Excelencia 'María de Maeztu').

Based on observations obtained with Planck (<http://www.esa.int/Planck>), an ESA science mission with instruments and contributions directly funded by ESA Member States, NASA, and Canada.

Funding for SDSS-III has been provided by the Alfred P. Sloan Foundation, the Participating Institutions, the National Science Foundation, and the U.S. Department of Energy Office of Science. The SDSS-III web site is <http://www.sdss3.org/>. SDSS-III is managed by the Astrophysical Research Consortium for the Participating Institutions of the SDSS-III Collaboration including the University of Arizona, the Brazilian Participation Group, Brookhaven National Laboratory, Carnegie Mellon University, University of Florida, the French Participation Group, the German Participation Group, Harvard University, the Instituto de Astrofísica de Canarias, the Michigan State/Notre Dame/JINA Participation Group, Johns Hopkins University, Lawrence Berkeley National Laboratory, Max Planck Institute for Astrophysics, Max Planck Institute for Extraterrestrial Physics, New Mexico State University, New York University, Ohio State University, Pennsylvania State University, University of Portsmouth, Princeton University, the Spanish Participation Group, University of Tokyo, University of Utah, Vanderbilt University, University of Virginia, University of Washington, and Yale University.

This research used resources of the National Energy Research Scientific Computing Center, which is supported by the Office of Science of the U.S. Department of Energy under Contract No. DEAC02-05CH11231. Power spectrum computations were supported by the facilities and staff of the UK Sciama High Performance Computing cluster supported by SEPNet and the University of Portsmouth. Power spectrum calculations, and fitting made use of the COSMOS/Universe supercomputer, a UK-CCC facility supported by HEFCE and STFC in cooperation with CGI/Intel.

The Science, Technology and Facilities Council is acknowledged for support through the Survey Cosmology and Astrophysics consolidated grant, ST/I001204/1.

AJC thanks the hospitality of the Institute of Cosmology & Gravitation at the University of Portsmouth, where this project was conceived.

REFERENCES

- Alam S. et al., 2015, *ApJS*, 219, 12
 Albrecht A. et al., 2006, *ArXiv Astrophysics e-prints*, astro-ph/0609591
 Anderson L. et al., 2014, *MNRAS*, 441, 24
 Anderson L. et al., 2016, in preparation
 Anderson L. et al., 2012, *MNRAS*, 427, 3435
 Aubourg É. et al., 2015, *Phys. Rev. D*, 92, 123516
 Betoule M. et al., 2014, *A&A*, 568, A22
 Beutler F. et al., 2011, *MNRAS*, 416, 3017
 Beutler F., Blake C., Koda J., Marín F. A., Seo H.-J., Cuesta A. J., Schneider D. P., 2016, *MNRAS*, 455, 3230
 Blake C. et al., 2011, *MNRAS*, 418, 1707
 Bolton A. S. et al., 2012, *AJ*, 144, 144
 Bull P., Ferreira P. G., Patel P., Santos M. G., 2015, *ApJ*, 803, 21
 Cole S. et al., 2005, *MNRAS*, 362, 505
 Crocce M., Scoccimarro R., 2008, *Phys. Rev. D*, 77, 023533
 Cuesta A. J., Verde L., Riess A., Jimenez R., 2015, *MNRAS*, 448, 3463
 Dawson K. S. et al., 2015, *ArXiv e-prints*, arXiv:1508.04473
 Dawson K. S. et al., 2013, *AJ*, 145, 10
 Delubac T. et al., 2015, *A&A*, 574, A59
 Eisenstein D. J., Hu W., 1998, *ApJ*, 496, 605
 Eisenstein D. J., Seo H.-J., Sirko E., Spergel D. N., 2007, *ApJ*, 664, 675
 Eisenstein D. J., Seo H.-J., White M., 2007, *ApJ*, 664, 660
 Eisenstein D. J. et al., 2011, *AJ*, 142, 72
 Eisenstein D. J. et al., 2005, *ApJ*, 633, 560
 Feldman H. A., Kaiser N., Peacock J. A., 1994, *ApJ*, 426, 23
 Font-Ribera A. et al., 2014a, *J. Cosmology Astropart. Phys.*, 5, 27
 Font-Ribera A., McDonald P., Mostek N., Reid B. A., Seo H.-J., Slosar A., 2014b, *J. Cosmology Astropart. Phys.*, 5, 23
 Gil-Marín H. et al., 2016, *ArXiv e-prints*, arXiv:1509.06373
 Gunn J. E. et al., 2006, *AJ*, 131, 2332
 Hartlap J., Simon P., Schneider P., 2007, *A&A*, 464, 399
 Heavens A., Jimenez R., Verde L., 2014, *Physical Review Letters*, 113, 241302
 Hill G. J. et al., 2008, in *Astronomical Society of the Pacific Conference Series*, Vol. 399, *Panoramic Views of Galaxy Formation and Evolution*, Kodama T., Yamada T., Aoki K., eds., p. 115
 Kazin E. A. et al., 2014, *MNRAS*, 441, 3524
 Kitaura F.-S. et al., 2015, *ArXiv e-prints*, arXiv:1509.06400
 Kitaura F.-S., Yepes G., Prada F., 2014, *MNRAS*, 439, L21
 Landy S. D., Szalay A. S., 1993, *ApJ*, 412, 64
 Laureijs R., 2009, *ArXiv e-prints*, arXiv:0912.0914
 Laureijs R. et al., 2011, *ArXiv e-prints*, arXiv:1110.3193
 Levi M. et al., 2013, *ArXiv e-prints*, arXiv:1308.0847
 Lewis A., Bridle S., 2002, *Phys. Rev. D*, 66, 103511
 Lewis A., Challinor A., Lasenby A., 2000, *ApJ*, 538, 473
 LSST Dark Energy Science Collaboration, 2012, *ArXiv e-prints*, arXiv:1211.0310
 Mostek N. et al., 2012, in *Society of Photo-Optical Instrumentation Engineers (SPIE) Conference Series*, Vol. 8446, *Society of Photo-Optical Instrumentation Engineers (SPIE) Conference Series*, p. 0
 Padmanabhan N., Xu X., Eisenstein D. J., Scalzo R.,

- Cuesta A. J., Mehta K. T., Kazin E., 2012, *MNRAS*, 427, 2132
- Percival W. J. et al., 2014, *MNRAS*, 439, 2531
- Planck Collaboration et al., 2015a, ArXiv e-prints, arXiv:1502.01582
- Planck Collaboration et al., 2014, *A&A*, 571, A16
- Planck Collaboration et al., 2015b, ArXiv e-prints, arXiv:1502.01589
- Planck Collaboration et al., 2015c, ArXiv e-prints, arXiv:1507.02704
- Reid B. et al., 2016, *MNRAS*, 455, 1553
- Ross A. J. et al., 2016, in preparation
- Ross A. J. et al., 2012, *MNRAS*, 424, 564
- Ross A. J., Samushia L., Howlett C., Percival W. J., Burden A., Manera M., 2015, *MNRAS*, 449, 835
- Schlegel D., White M., Eisenstein D., 2009, in *Astronomy, Vol. 2010, astro2010: The Astronomy and Astrophysics Decadal Survey*, p. 314
- Smee S. A. et al., 2013, *AJ*, 146, 32
- Spergel D. et al., 2013a, ArXiv e-prints, arXiv:1305.5425
- Spergel D. et al., 2013b, ArXiv e-prints, arXiv:1305.5422
- Suzuki N. et al., 2012, *ApJ*, 746, 85
- Tojeiro R. et al., 2014, *MNRAS*, 440, 2222
- Vargas-Magaña M. et al., 2016, in preparation
- Vargas-Magaña M., Ho S., Fromenteau S., Cuesta A. J., 2015, ArXiv e-prints, arXiv:1509.06384
- White M., Tinker J. L., McBride C. K., 2014, *MNRAS*, 437, 2594
- Xu X., Cuesta A. J., Padmanabhan N., Eisenstein D. J., McBride C. K., 2013, *MNRAS*, 431, 2834